

Cite this: *Chem. Sci.*, 2024, 15, 6860

All publication charges for this article have been paid for by the Royal Society of Chemistry

An anthraquinone-based bismuth–iron metal–organic framework as an efficient photoanode in photoelectrochemical cells†

Cai Shi,^a Miguel Gomez-Mendoza,^b Eloy Gómez de Oliveira,^a Miguel García-Tecedor,^b Mariam Barawi,^b Fátima Esteban-Betegón,^a Marta Liras,^b Enrique Gutiérrez-Puebla,^b Angeles Monge,^a Víctor A. de la Peña O'Shea^{*b} and Felipe Gándara^{ib*ab}

Metal–organic frameworks (MOFs) are appealing candidate materials to design new photoelectrodes for use in solar energy conversion because of their modular nature and chemical versatility. However, to date there are few examples of MOFs that can be directly used as photoelectrodes, for which they must be able to afford charge separation upon light absorption, and promote the catalytic dissociation of water molecules, while maintaining structural integrity. Here, we have explored the use of the organic linker anthraquinone-2, 6-disulfonate (2, 6-AQDS) for the preparation of MOFs to be used as photoanodes. Thus, the reaction of 2, 6-AQDS with Bi(III) or a combination of Bi(III) and Fe(III) resulted in two new MOFs, BiPF-10 and BiFePF-15, respectively. They display similar structural features, where the metal elements are disposed in inorganic-layer building units, which are pillared by the organic linkers by coordination bonds through the sulfonic acid groups. We show that the introduction of iron in the structure plays a crucial role for the practical use of the MOFs as a robust photoelectrode in a photoelectrochemical cell, producing as much as 1.23 mmol H₂ cm^{−2} with the use of BiFePF-15 as photoanode. By means of time-resolved and electrochemical impedance spectroscopic studies we have been able to unravel the charge transfer mechanism, which involves the formation of a radical intermediate species, exhibiting a longer-lived lifetime by the presence of the iron-oxo clusters in BiFePF-15 to reduce the charge transfer resistance.

Received 9th February 2024

Accepted 27th March 2024

DOI: 10.1039/d4sc00980k

rsc.li/chemical-science

Introduction

Within the current environmental and energy crisis that our society is facing, there is clearly a pressing need to develop and deploy new materials and technologies that will allow us to implement alternative sustainable energy sources. Hydrogen, as an energy vector, is arguably playing an essential role in the transition from the use of fossil fuels to clean and renewable energies. However, it is essential that hydrogen production is sustainably achieved, for which solar powered photoelectrochemical cells (PECs) are highly attractive, since they exploit sun light for the electrocatalytic rupture of water

molecules to generate hydrogen. To achieve this goal, highly photoactive materials with adequate transport properties are required to be used as photoelectrodes in PECs.

These materials must be able to efficiently harvest solar energy for electron–hole charge separation, followed by charge migration to the surface where the molecules react. To this end, several classes of materials are currently being investigated as photoelectrodes for solar energy conversion and hydrogen production, such as metal oxides, organic polymers, or hybrid organo–inorganic materials.¹ Metal–organic frameworks, MOFs, are a class of materials formed by combining metal atoms and organic linkers through strong coordination bonds to create robust, periodic structures. Thanks to their enormous structural, topological, and chemical versatility, MOFs are being widely investigated in numerous fields. Thus, the modular nature of MOFs allows a rational selection of their building components to modify their activity for the selected application, ranging from gas separation,² water harvesting,³ drug delivery,^{4,5} or heterogeneous catalysis,⁶ including photo-^{7,8} and photoelectrocatalysis.⁹ Thus, we previously demonstrated that a judiciously selected organic linker plays a central role in the photoelectrocatalytic hydrogen production.¹⁰ In particular, we

^aMaterials Science Institute of Madrid – Spanish National Research Council, Sor Juana Inés de la Cruz, 3, 28049, Madrid, Spain. E-mail: gandara@icmm.csic.es

^bPhotoactivated Processes Unit, IMDEA Energy Institute, Móstoles Technology Park, Avenida Ramón de la Sagra 3, Móstoles, 28935, Madrid, Spain. E-mail: victor.delapenya@imdea.org

† Electronic supplementary information (ESI) available: Full experimental procedures, spectra, and analytical data is provided. CCDC for BiPF-10 and BiFePF-15 have been deposited in the CCDC with numbers 2267791 and 2268781, respectively. For ESI and crystallographic data in CIF or other electronic format see DOI: <https://doi.org/10.1039/d4sc00980k>



Scheme 1 Single- and bimetal MOFs have been synthesized with the same anthraquinone based linker.

found that a bismuth MOF incorporating a hole-transport linker produced hydrogen through a process involving the formation of an anionic radical intermediate. Following up, we have now synthesized two new MOFs with the use of anthraquinone-2, 6-disulfonic acid (2, 6-AQDS) as organic linker (Scheme 1). We have selected the commercially available 2, 6-AQDS linker due the rich redox chemistry of anthraquinones, which in addition are well-known to form radical species¹¹ under photoexcitation.^{12,13} We have also continued to focus on bismuth MOFs,^{14,15} which are recently receiving increasing interest due to the low-toxicity and high natural abundance of this metal element.¹⁶

Bismuth MOFs based on sulfonate linkers have already been reported,^{17–19} and the rich coordination chemistry of this element results in a large number of possible coordination environments and secondary building units when it is incorporated into MOF networks,^{20–22} a determinant factor in the materials' chemical stability and robustness.²³ Herein, we also

demonstrate that the modification and adjustment of the inorganic part of the MOF by combining different metal elements, namely bismuth and iron leads to a remarkable improvement in the stability and activity of the materials when used for hydrogen generation in a PECs. The selection of iron is motivated by the versatile photoredox chemistry of this highly abundant and non-toxic element. Thus, the two newly reported compounds own structures consisting of inorganic metal-sulfonate layers, pillared by the anthraquinone moieties. However, only the multi-metal MOF containing both bismuth and iron in the layers exhibits the required stability and robustness during the photoelectrochemical reactions, reaching photocurrent density values as high as 0.03 mA cm^{−2}. As a proof of concept to demonstrate the potential of the materials as photoanode, we show that up to 1.23 mmol H₂ cm^{−2} h^{−1} are produced in a PECs with BiFePF-15 as anode.

Results and discussion

The first of the newly reported compounds, denoted BiPF-10, was synthesized through the reaction of bismuth nitrate with 2, 6-AQDS disodium salt (Scheme 1). The chemical formula of the compound according to the single-crystal determined structure is [Bi(OH)(AQDS)(H₂O)], which is consistent with the results of the chemical elemental analysis of the bulk sample (calc. C: 27.55%, H: 1.49%, S: 10.51%, exp. C: 27.33%, H: 1.68%, S: 10.37%). BiPF-10 crystallizes in the triclinic *P* $\bar{1}$ space group. Bismuth atoms,

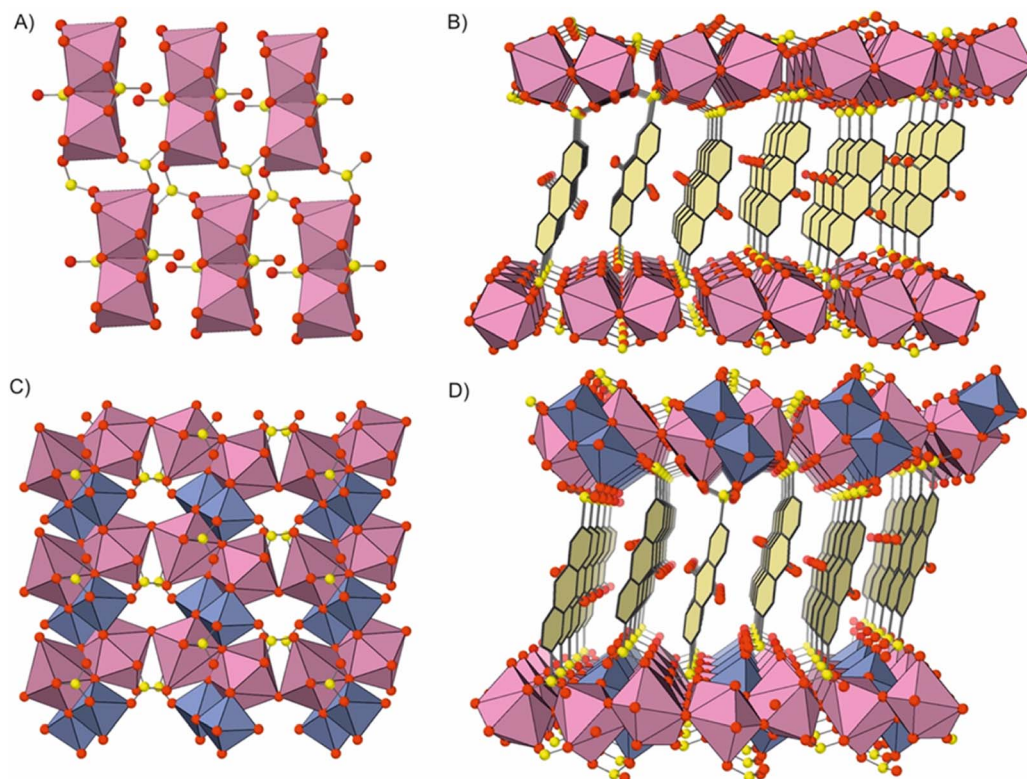


Fig. 1 Single-crystal X-ray diffraction structure representation of layer and full structure of (A and B) BiPF-10 and (C and D) BiFePF-15. Color scheme: bismuth and iron are magenta and blue polyhedra, respectively. Sulfur and oxygen atoms are yellow and red balls, and carbon atoms are represented as black sticks. Hydrogen atoms are omitted for clarity.



with coordination number eight, are arranged forming $[\text{Bi}_2(\text{OH})_2(\text{H}_2\text{O})_2(\text{SO}_3)_2]$ dimeric units, which are further linked together through six bridging sulfonate groups (Fig. 1a), creating two-dimensional layered inorganic secondary building units,²⁴ which are pillared by the anthraquinone molecules (Fig. 1b). The synthesis of the second compound, denoted BiFePF-15, was carried out in one step, by mixing bismuth and iron nitrate along with $\text{Na}_2(2, 6\text{-AQDS})$. The compound crystallizes in the monoclinic $C2/c$ space group. Inorganic layers are similarly formed in BiFePF-15, consisting of bismuth and iron cations coordinated to oxygen atoms (Fig. 1c). Bismuth atoms are also in coordination number eight, with Bi–O bond distances ranging from 2.154(12) Å to 3.078(2) Å, while iron atoms are octahedrally coordinated, with Fe–O distances ranging from 1.920(1) Å to 2.093(1) Å. The inorganic layers are formed with the metal-coordination polyhedra hold together through $\mu\text{-O}$ and $\mu^3\text{-O}$ atoms, and through sulfonate groups. The anthraquinone molecules connect the inorganic layers forming the three-dimensional structure. Noting that the position of the hydrogen atoms cannot be determined from the single crystal diffraction data analysis, the $\mu\text{-O}$ and $\mu^3\text{-O}$ atoms might belong to OH^- , O^{2-} , or OH_2 species. Based on bond distances and angles, and charge neutrality considerations, we have attributed the $\mu\text{-O}$ atom that is bridging two bismuth atoms as a water ligand, the $\mu\text{-O}$ bridging bismuth and iron atoms as OH^- , while the $\mu^3\text{-O}$ atom bridging one Bi, Fe, and Fe, as OH^- , and the $\mu^3\text{-O}$ bridging Bi, Bi, and Fe as O^{2-} . To support this assignment, we completed a DFT based optimization including the hydrogen atoms at these locations, and the resulting optimized structure is in good agreement with the experimentally determined one (Fig. S1†). Therefore, the MOF chemical formula is determined to be $[\text{Bi}_2\text{Fe}_2(\text{OH})_4\text{O}_2(\text{H}_2\text{O})(\text{AQDS})_2]$, which is also in agreement with the results of the bulk sample C, H, S elemental analysis (exp. C: 23.81%, H: 1.26%, S: 9.06%, calc. C: 24.09%, H: 1.30%, S: 9.19%) and inductively coupled plasma atomic emission spectroscopy (exp. Bi: 32%, Fe: 7.0%, calc. Bi: 30%, Fe: 8.1%).

The powder X-ray diffraction (PXRD) patterns of BiPF-10 and BiFePF-15 match the ones calculated from the single crystal determined structures, and demonstrate the phase purity of the samples (Fig. S2†), which is also supported by the SEM images, where homogeneously shaped crystals were observed (Fig. S3A and B†). In the case of BiFePF-15, EDS results were also in agreement with the proposed formula (Fig. S3C†), evidencing the presence of both bismuth and iron in the BiFePF-15 crystals. The thermal stability of BiPF-10 and BiFePF-15 was investigated by thermo-gravimetric analysis (TGA), showing that the materials are thermally stable up to above 400 °C (Fig. S4A and B†).

The UV-vis diffuse reflectance spectra collected for the solid samples was used to investigate the absorption range and the optical band gaps of BiPF-10 and BiFePF-15 (Fig. S5†). Compared with BiPF-10, BiFePF-15 exhibited a broader absorption across the UV-vis spectral range (Fig. S5A†). By means of Tauc-plot method the band gap energy of BiPF-10 and BiFePF-15 were determined as a direct transition (*ca.* 2.8 and 2.6 eV, respectively, Fig. S5B†), and showing the effect of presence of iron in the structure.

Following, we tested the photoelectrochemical activity of both materials. The negative value of the photopotential

measurements (Fig. S6†) under open circuit conditions is indicative of the photoactive and a n-type semiconducting behavior of both BiPF-10 and BiFePF-15. To ensure that the materials are stable under the conditions required for the photoelectrochemical studies, the PXRD patterns of both MOFs were collected after being soaked in a 0.5 M Na_2SO_3 aqueous solution (pH = 9), which is the selected electrolyte and hole scavenger during hydrogen evolution reaction (HER) with PEC. Remarkably, BiFePF-15 did not show any significant change in the peaks position or intensity (Fig. S7B†). In addition, SEM images (Fig. S7C†) did not show any obvious sample degradation. On the contrary, the PXRD pattern of BiPF-10 after being soaked for 1 h already shows a marked loss of crystallinity, and after 3 h, no signals of the original pattern are visible (Fig. S7A†). Thus, the use of BiPF-10 as photoelectrode is hampered by its limited chemical stability under photoelectrochemical working conditions. On the contrary, the incorporation of iron atoms into the inorganic SBU seems to play a stabilizing role of the structure. Thus, BiFePF-15 demonstrates to be structurally robust and chemically stable for use in PECs. Moreover, the photovoltage measurements (Fig. S6†) of these two systems reveals the higher photoresponse and a much faster charge transfer of BiFePF-15, indicative of the active role of iron atoms. Linear sweep voltammetry under chopped illumination test shows positive values of the photocurrent (Fig. 2A), supporting the prospective use of BiFePF-15 as photoanode in a PEC process.²⁵ In addition, the chronoamperometry curve recorded with a 1.0 V bias potential *vs.* reversible hydrogen electrode (RHE) (Fig. 2B) shows the stability of BiFePF-15, reaching photocurrent densities of *ca.* 0.03 mA cm^{-2} after 3600 s, and a drop of the current to zero when light is off.

We also performed electrochemical impedance spectroscopy (EIS) measurements under dark and illumination conditions with BiFePF-15 to investigate the changes in the charge transfer resistance of the analyzed material–electrolyte interface. Fig. 2C shows the Nyquist plots acquired at 1.0 V *vs.* RHE, where the material shows the higher photoresponse previous to the rise of the dark current. As expected for a photoelectrode, the measured semicircle is clearly smaller under illumination than the one recorded under dark conditions at the same applied bias. The observed difference is indicative of a drastic decrease in the charge transfer resistance, associated with an enhanced charge transfer at the BiFePF-15/electrolyte interface of the photogenerated holes under anodic conditions.²⁶

Encouraged by these results, we proposed a proof of concept for photoelectrochemical H_2 generation using BiFePF-15 as photoanode. This photoelectrochemical measurements were carried out under simulated 1 Sun solar irradiation (AM 1.5) during a chronoamperometry at 1.0 V *vs.* RHE. The PEC cell was connected to a gas chromatograph (GC), and an argon current of 50 $\text{cm}^3 \text{STP min}^{-1}$ flow through the cell was employed both to purge and to remove the gas inside and carry the reaction products to GC. A hydrogen flow was detected upon irradiation, showing a constant evolution, and reaching an accumulated value of 1.23 mmol cm^{-2} after 1 h irradiation and start to decrease after switching off the lamp (Fig. 2D). This result supports the potential of BiFePF-15 as photoanode in a PEC,



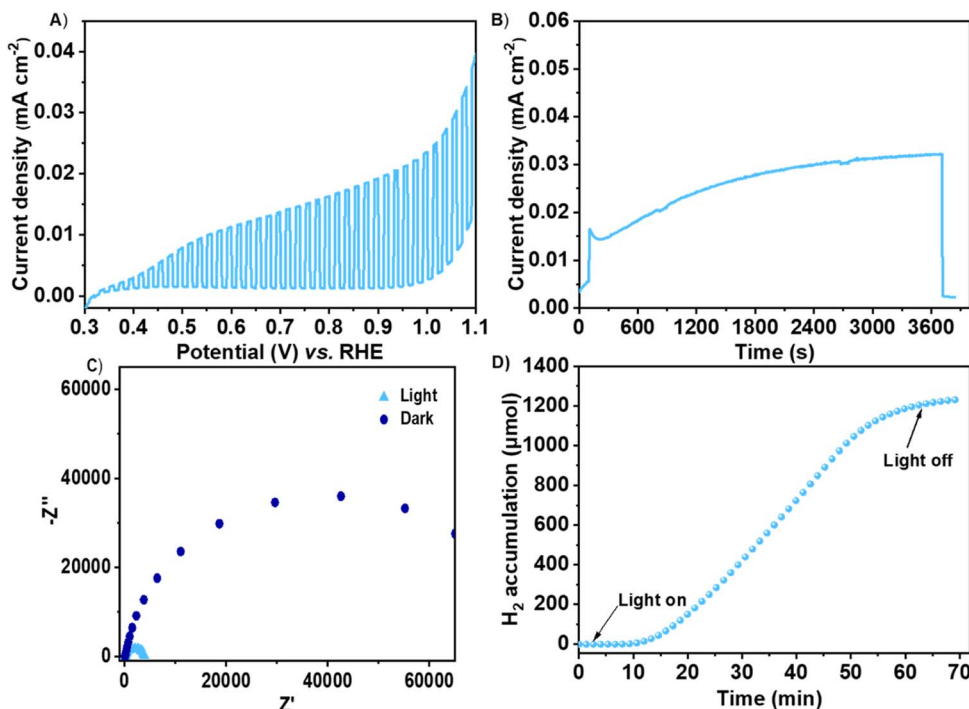


Fig. 2 (A) Linear sweep voltammetry under chop illumination, (B) chronoamperometry curve recorded at 1.0 V potential vs. RHE. Light was off after 3600 s, producing the sudden drop in current. (C) Electrochemical impedance spectra under dark and light, and (D) accumulated hydrogen production in a PEC with BiFePF-15 as photoanode, at 1.0 V potential vs. RHE.

and it is among the few reported examples of bare MOFs employed as photoelectrodes.^{10,27–30}

To understand the observed photoelectrochemical performance and the kinetic implications on the overall reaction pathways, we have completed a set of photophysical studies. We first recorded the photoluminescence spectra of the MOFs, and compared with that of the organic 2, 6-AQDS linker. As shown in Fig. S5C,† there is a marked decrease in the intensity of the emission signals of the MOFs, as compared to the linker, indicating a slower radiative recombination rate of the photo-generated carriers for BiFePF-15 and BiPF-10, especially for BiFePF-15.³¹ The decay traces (Fig. S5D)† were used to estimate the lifetime values, finding that they are shorter for the organic linker (1.68 ns) and BiPF-10 (2.54 ns) than for BiFePF-15 (4.50 ns), in good agreement with the photoluminescence results.

In addition, we performed nanosecond transient absorption spectroscopy (TAS) experiments. Measurements were registered both in absence and presence of Na₂SO₃ aqueous solution under inert atmosphere, to ensure comparable conditions to those employed for H₂ production experiments. For the measurements in absence of sulfite see Fig. S8–S12.† TAS experiments in the presence of Na₂SO₃ as sacrificial agent were carried out to investigate the intermediates involved in the photocatalytic reactions (Fig. 3A and S13–S17)†. In the presence of Na₂SO₃, we observe for BiPF-10 and BiFePF-15 transient absorption peaks between 350–425 nm (with maximum at 385 nm) and 450–550 nm (with maximum at 520 nm) (Fig. 3A, S14, S15 and S17)†. These characteristic bands were also observed for the naked ligand (Fig. S13)† and are consistent with

previously reported anion radical 2, 6-AQDS^{•−} (and other AQ derivatives).^{32–34} Both MOFs showed a more intense absorption band at 385 and 520 nm (Fig. S17)† than the naked ligand while keeping the same ratio between both peaks, indicative of the same transient species 2, 6-AQDS^{•−} in all spectral range. This transient species exhibited much longer τ for BiFePF-15 (273 μ s for its maximum at 520 nm calculated from the first slope of the curve, Fig. S15D)† than BiPF-10 (\sim 100 μ s, Fig. S14D)† or the ligand (\sim 80 μ s, Fig. S13D)† under inert atmosphere (Fig. 3B and S16)†. Here, Fe–O units in BiFePF-15 plays an important role to enhance the photocurrent and reduces the charge transfer resistance (Fig. 2) and promote a noteworthy slow-down of the electron–hole pair recombination for BiFePF-15, which remains active even above 600 μ s after pulse (Fig. S15A)†. Related finding has been reported for iron containing MOFs,^{35,36} which are also known to directly excite upon visible light irradiation due to the existence of Fe–O clusters.³⁷ All these characteristic, besides its intrinsic chemical stability (Fig. S7)†, help to explain the enhancement in the efficiency for BiFePF-15 under visible light (Fig. 2). In general, AQ and its derivatives form colored radical anions upon single-electron reduction, which can be used for photocatalytic transformations.^{38,39} This is also observed at eye-catching in our samples, which upon UV light exposure leads to a color change from yellow to orange-red (Fig. 3C). The optoelectronic properties of BiFePF-15 were then calculated using Time Dependent Density Functional Theory (TD-DFT). Regarding the electronic structure of the BiFePF-15 MOF, the total density of states (DOS), Fig. 4, shows that the valence band maximum (VBM) is composed by O 2p states hybridized with Fe



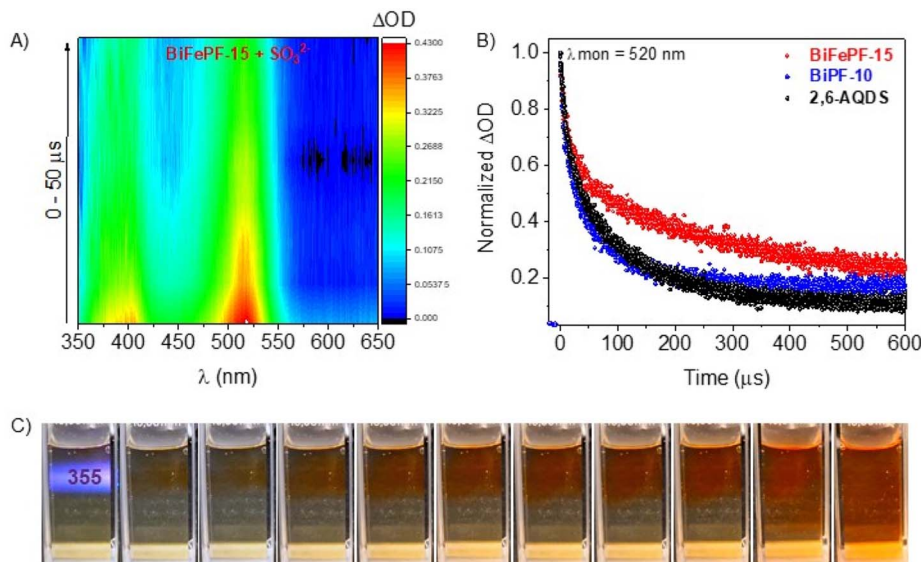


Fig. 3 (A) 2D mapping of the transient absorption spectra ($\lambda_{\text{exc}} = 355$ nm) of BiFePF-15 in the presence of 0.5 M Na_2SO_3 at different timescales under N_2 . (B) Comparative of the normalized transient decay traces after laser excitation at $\lambda_{\text{exc}} = 355$ nm ($\lambda_{\text{mon}} = 520$ nm) for 2, 6-AQDS ligand, BiPF-10 and BiFePF-15 MOFs in the presence of aqueous 0.5 M Na_2SO_3 under N_2 . (C) The color change of BiFePF-15 suspension in presence of 0.5 M Na_2SO_3 at different timescale (0–30 s, left to right) upon UV light (355 nm) exposure.

3d and Bi 6s 6p orbitals, while the conduction band minimum (CBM) is mainly formed by Fe d 2p and Bi 6s 6p orbitals, both separated by an estimated band gap of 2.45 eV. These results indicate that the electronic transitions in the range 350–470 nm, characteristic of photocatalytic experiments, are associated with ligand-to-metal charge-transfer (LMCT) excitations from oxygen to iron atoms.⁴⁰ The main light driven electronic transition are located in the anthraquinone and from them to iron atoms. The calculated excitation energies and molecular orbitals contributing to this LMCT are shown in Fig. S18.† This suggests a possible photo-reduction of Fe^{3+} to higher electron density species ($\text{Fe}^{\delta+}$). The LMCT process is then followed by the triplet deactivation to generate the corresponding radical anion (Fig. 3C and S13–S17†).

Based on the combination of these experimental results, we can propose a reaction mechanism, which explains the involvement of charge-/electron-transfer processes in photocatalytic H_2 production. Upon light absorption (fs timescale), BiFePF-15 undergoes a charge separation. This generates a singlet excited state ($^1\text{BiFePF-15}^*$, with PL lifetime of 4.50 ns) that undergoes a triplet excited state ($^3\text{BiFePF-15}^*$), by intersystem crossing. The presence of iron in the SBU improves the charge separation efficiency and the lifetime of the transient species, which is playing a key role in the reaction process. The hole scavenger (SO_3^{2-}) interacts with the MOF, injecting charge into the framework with the subsequent formation of a radical anion intermediate state ($\text{BiFePF-15}^{\cdot-}$), which has a lifetime over 273 μs . Finally, BiFePF-15 radical anion transfers electrons to the electrode where the redox cycle is closed by H_2 evolution reaction.

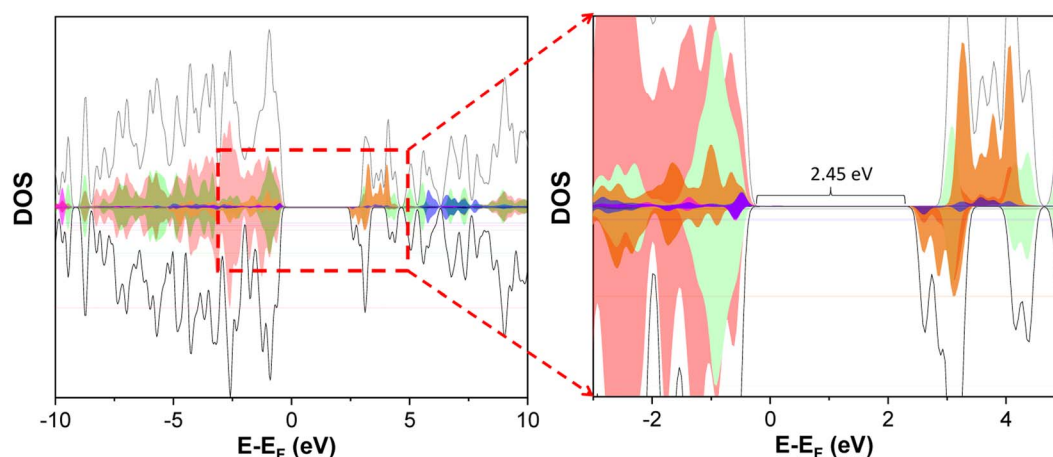


Fig. 4 Density of states (DOS), DOS colours: Fe 3d (Orange), Bi 6s (magenta), Bi 6p (blue) and O 2p (red light) C 2p (green light).



Conclusions

In summary, here we have demonstrated the suitability of the use of anthraquinone based linkers to synthesize photoactive MOFs for direct use as photoanodes in PECs. In particular, the choice of a mixed-metal system based on the combination of iron and bismuth with 2, 6-AQDS affords a highly stable material, with broadened visible light response and enhanced charge separation efficiency, which results in an increase in the radical anion lifetime in the presence of sacrificial agents, and consequently, in a high activity in a photoelectrochemical cell for hydrogen production, being among the largest reported for bare MOFs as photoactive materials.[‡]

Data availability

All experimental procedures, spectroscopic data, and all the relevant data generated and analysed are available in the manuscript and ESI.[†] The detailed crystallographic information can be found in ESI,[†] and the crystallographic data with CCDC number 2267791 and 2268781 for BiPF-10 and BiFePF-15, respectively, are available *via* CCDC.

Author contributions

C. S. synthesized BiFePF-15, wrote the original draft of the manuscript and performed experimental tests except TAS. M. G. M. performed and interpreted TAS experiments. E. G. O. prepared BiPF-10. Photoelectrochemical tests were supported from M. G. T. and M. B., F. E. B., E. G. P. and A. M. contributed to the SCXRD analyses. M. L. conducted the PL measurement. V. A. P. O. and F. G. directed the study, performed TD-DFT and single crystal analysis. All authors discussed the results and contributed to the final version of the manuscript.

Conflicts of interest

There are no conflicts to declare.

Acknowledgements

C. S. thanks the China Scholarship Council (CSC) for a scholarship. This work has received financial support through projects PID2021-123287OB-I00, PID2022-141688OB-I00, TED2021-129999A-C33, NovaCO2 (PID2020-118593RB-C22) and SolarCPP-Bat (CNS2022-135380) funded by MCIN/AEI/10.13039/501100011033/and ERDF A way to make Europe and PLEC2021-007906 (SOLFUTURE) funded by MCIN/AEI/10.13039/501100011033 and European Union NextGenerationEU/PRTR. M. B. Thanks the Spanish MICIN the RYC2022-038157-I grant funded by MCIN/AEI/10.13039/501100011033. The project that gave rise to these results received the support of a fellowship from "la Caixa" Foundation (ID 100010434). The fellowship code is LCF/BQ/PR23/11980046.

Notes and references

[‡] The authors have cited additional references within the ESI regarding extended discussion of the TAS experiments.^{41–50}

- 1 M. Liras, M. Barawi and V. A. D. O'Shea, *Chem. Soc. Rev.*, 2019, **48**, 5454–5487.
- 2 S. J. Datta, A. Mayoral, N. M. S. Bettahalli, P. M. Bhatt, M. Karunakaran, I. D. Carja, D. Fan, P. G. M. Mileo, R. Semino, G. Maurin, O. Terasaki and M. Eddaoudi, *Science*, 2022, **376**, 1080.
- 3 Z. L. Zheng, N. Hanikel, H. Lyu and O. M. Yaghi, *J. Am. Chem. Soc.*, 2022, **144**, 22669–22675.
- 4 I. A. Lázaro, C. J. R. Wells and R. S. Forgan, *Angew. Chem., Int. Ed.*, 2020, **59**, 5211–5217.
- 5 F. D. Duman, A. Monaco, R. Foulkes, C. R. Becer and R. S. Forgan, *ACS Appl. Nano Mater.*, 2022, **5**, 13862–13873.
- 6 G. Zhou, Y. Wang and Z. Huang, *Chem Catal.*, 2022, **2**, 3304–3319.
- 7 S. Rojas, J. García-González, P. Salcedo-Abraira, I. Rincón, J. Castells-Gil, N. M. Padial, C. Marti-Gastaldo and P. Horcajada, *Sci. Rep.*, 2022, **12**, 14513.
- 8 A. García-Baldoví, R. Del Angel, G. Mouchaham, S. P. Liu, D. Fan, G. Maurin, S. Navalón, C. Serre and H. Garcia, *Energy Environ. Sci.*, 2023, **16**, 167–177.
- 9 R. Ifraimov, S. Mukhopadhyay and I. Hod, *Sol. RRL*, 2023, **7**, 2201068.
- 10 A. García-Sánchez, M. Gomez-Mendoza, M. Barawi, I. J. Villar-Garcia, M. Liras, F. Gándara and V. A. D. O'Shea, *J. Am. Chem. Soc.*, 2020, **142**, 318–326.
- 11 F. Gándara, N. Snejkó, A. de Andrés, J. R. Fernandez, J. C. Gómez-Sal, E. Gutierrez-Puebla and A. Monge, *RSC Adv.*, 2012, **2**, 949–955.
- 12 A. Harriman and A. Mills, *Photochem. Photobiol.*, 2008, **33**, 619–625.
- 13 J. N. Moore, D. Phillips, N. Nakashima and K. Yoshihara, *J. Chem. Soc., Faraday Trans.*, 1986, **82**, 745.
- 14 Q. X. Wang and G. Li, *Inorg. Chem. Front.*, 2021, **8**, 572–589.
- 15 Z. Wang, Z. Zeng, H. Wang, G. Zeng, P. Xu, R. Xiao, D. Huang, S. Chen, Y. He, C. Zhou, M. Cheng and H. Qin, *Coord. Chem. Rev.*, 2021, **439**, 213902.
- 16 E. S. Grape, J. G. Flores, T. Hidalgo, E. Martínez-Ahumada, A. Gutiérrez-Alejandre, A. Hautier, D. R. Williams, M. O'Keeffe, L. Öhrström, T. Willhammar, P. Horcajada, I. A. Ibarra and A. K. Inge, *J. Am. Chem. Soc.*, 2020, **142**, 16795–16804.
- 17 M. Albat and N. Stock, *Inorg. Chem.*, 2018, **57**, 10352–10363.
- 18 E. P. Gómez-Oliveira, N. Méndez, M. Iglesias, E. Gutiérrez-Puebla, L. M. Aguirre-Díaz and M. Á. Monge, *Inorg. Chem.*, 2022, **61**, 7523–7529.
- 19 M. Albat, A. K. Inge and N. Stock, *Z. Kristallogr.-Cryst. Mater.*, 2017, **232**, 245–253.
- 20 M. Köppen, V. Meyer, J. Ångström, A. K. Inge and N. Stock, *Cryst. Growth Des.*, 2018, **18**, 4060–4067.
- 21 M. Köppen, O. Beyer, S. Wuttke, U. Luning and N. Stock, *Dalton Trans.*, 2017, **46**, 8658–8663.



- 22 T. Rhauderwiek, C. dos Santos Cunha, H. Terraschke and N. Stock, *Eur. J. Inorg. Chem.*, 2018, **2018**, 3232–3240.
- 23 E. P. Gómez-Oliveira, D. Reinares-Fisac, L. M. Aguirre-Díaz, F. Esteban-Betegón, M. Pintado-Sierra, E. Gutiérrez-Puebla, M. Iglesias, M. A. Monge and F. Gándara, *Angew. Chem., Int. Ed.*, 2022, **61**, e202209335.
- 24 S. Kampouri, M. X. Zhang, T. Y. Chen, J. J. Oppenheim, A. C. Brown, M. T. Payne, J. L. Andrews, J. L. Sun and M. Dinca, *Angew. Chem., Int. Ed.*, 2022, **61**, e202213960.
- 25 J. Barrio, C. Gibaja, M. García-Tecedor, L. Abisdris, I. Torres, N. Karjule, S. Giménez, M. Shalom and F. Zamora, *Appl. Mater. Today*, 2020, **20**, 100714.
- 26 L. Collado, M. Gomez-Mendoza, M. García-Tecedor, F. E. Oropeza, A. Reynal, J. R. Durrant, D. P. Serrano and V. A. D. O'Shea, *Appl. Catal., B*, 2023, **324**, 122206.
- 27 R. Ifraemov, R. Shimon, W. He, G. Peng and I. Hod, *J. Mater. Chem. A*, 2019, **7**, 3046–3053.
- 28 N. M. Padial, J. Castells-Gil, N. Almora-Barrios, M. Romero-Angel, I. da Silva, M. Barawi, A. Garcia-Sanchez, V. A. de la Pena O'Shea and C. Marti-Gastaldo, *J. Am. Chem. Soc.*, 2019, **141**, 13124–13133.
- 29 Y. N. Gong, T. Ouyang, C. T. He and T. B. Lu, *Chem. Sci.*, 2016, **7**, 1070–1075.
- 30 Y. Lu, H. Zhong, J. Li, A. M. Dominic, Y. Hu, Z. Gao, Y. Jiao, M. Wu, H. Qi, C. Huang, L. J. Wayment, U. Kaiser, E. Spiecker, I. M. Weidinger, W. Zhang, X. Feng and R. Dong, *Angew. Chem., Int. Ed.*, 2022, **61**, e202208163.
- 31 M. Barawi, M. Gomez-Mendoza, F. E. Oropeza, G. Gorni, I. J. Villar-Garcia, S. Gimenez, V. A. D. O'Shea and M. Garcia-Tecedor, *ACS Appl. Mater. Interfaces*, 2022, **14**, 33200–33210.
- 32 J. Hankache and O. S. Wenger, *Chem. Commun.*, 2011, **47**, 10145–10147.
- 33 F. D. Lewis, A. K. Thazhathveetil, T. A. Zeidan, J. Vura-Weis and M. R. Wasielewski, *J. Am. Chem. Soc.*, 2010, **132**, 444–445.
- 34 A. Mau and W. Sasse, *Aust. J. Chem.*, 1982, **35**, 1723.
- 35 K. G. M. Laurier, E. Fron, P. Atienzar, K. Kennes, H. Garcia, M. Van der Auweraer, D. E. De Vos, J. Hofkens and M. B. J. Roefsaers, *Phys. Chem. Chem. Phys.*, 2014, **16**, 5044–5047.
- 36 Z. Y. Guan, S. B. Zhu, S. Ding, D. S. Xia and D. Y. Li, *Chemosphere*, 2022, **299**, 134481.
- 37 D. K. Wang and Z. H. Li, *Res. Chem. Intermed.*, 2017, **43**, 5169–5186.
- 38 B. R. Eggins and P. K. J. Robertson, *J. Chem. Soc., Faraday Trans.*, 1994, **90**, 2249.
- 39 P. Nelleborg, H. Lund and J. Eriksen, *Tetrahedron Lett.*, 1985, **26**, 1773–1776.
- 40 L. Collado, I. Jansson, A. E. Platero-Prats, V. Perez-Dieste, C. Escudero, E. Molins, L. C. I. Doucastela, B. Sánchez, J. M. Coronado, D. P. Serrano, S. Suarez and V. A. de la Pena-O'Shea, *ACS Catal.*, 2017, **7**, 1646–1654.
- 41 H. J. van Ramesdonk, B. H. Bakker, M. M. Groeneveld, J. W. Verhoeven, B. D. Allen, J. P. Rostron and A. Harriman, *J. Phys. Chem. A*, 2006, **110**, 13145–13150.
- 42 D. Sasikumar, A. T. John, J. Sunny and M. Hariharan, *Chem. Soc. Rev.*, 2020, **49**, 6122–6140.
- 43 S. Goia, M. A. P. Turner, J. M. Woolley, M. D. Horbury, A. J. Borrill, J. J. Tully, S. J. Cobb, M. Staniforth, N. D. M. Hine, A. Burris, J. V. Macpherson, B. R. Robinson and V. G. Stavros, *Chem. Sci.*, 2022, **13**, 486–496.
- 44 J. Hankache and O. S. Wenger, *Phys. Chem. Chem. Phys.*, 2012, **14**, 2685–2692.
- 45 K. Tickle and F. Wilkinson, *Trans. Faraday Soc.*, 1965, **61**, 1981.
- 46 A. A. Lamola and G. S. Hammond, *J. Chem. Phys.*, 1965, **43**, 2129–2135.
- 47 P. R. Maddigapu, A. Bedini, C. Minero, V. Maurino, D. Vione, M. Brigante, G. Mailhot and M. Sarakha, *Photochem. Photobiol. Sci.*, 2010, **9**, 323–330.
- 48 I. Loeff, A. Treinin and H. Linschitz, *J. Phys. Chem.*, 1983, **87**, 2536–2544.
- 49 J. Metcalfe, *J. Chem. Soc., Faraday Trans. 1*, 1983, **79**, 1721.
- 50 R. Carmieli, A. L. Smeigh, S. M. M. Conron, A. K. Thazhathveetil, M. Fuki, Y. Kober, F. D. Lewis and M. R. Wasielewski, *J. Am. Chem. Soc.*, 2012, **134**, 11251–11260.

